CHEMISTRY

IrO$_x$·nH$_2$O with lattice water–assisted oxygen exchange for high-performance proton exchange membrane water electrolyzers

Jun Xu[1]†, Huanyu Jin[1,2]†, Teng Lu[3], Junsheng Li[4], Yun Liu[3], Kenneth Davey[1], Yao Zheng[1]*, Shi-Zhang Qiao[1]*

The trade-off between activity and stability of oxygen evolution reaction (OER) catalysts in proton exchange membrane water electrolyzer (PEMWE) is challenging. Crystalline IrO$_2$ displays good stability but exhibits poor activity; amorphous IrO$_x$ exhibits outstanding activity while sacrificing stability. Here, we combine the advantages of these two materials via a lattice water–incorporated iridium oxide (IrO$_x$·nH$_2$O) that has short-range ordered structure of hollandite-like framework. We confirm that IrO$_x$·nH$_2$O exhibits boosted activity and ultra-high stability of >5700 hours (~8 months) with a record-high stability number of 1.9×10^7 n$_{oxygen}$ n$_{Ir}^{-1}$. We evidence that lattice water is active oxygen species in sustainable and rapid oxygen exchange. The lattice water–assisted modified OER mechanism contributes to improved activity and concurrent stability with no apparent structural degradation, which is different to the conventional adsorbate evolution mechanism and lattice oxygen mechanism. We demonstrate that a high-performance PEMWE with IrO$_x$·nH$_2$O as anode electrocatalyst delivers a cell voltage of 1.77 V at 1 A cm^{-2} for 600 hours (60°C).

INTRODUCTION

Proton exchange membrane water electrolyzers (PEMWEs) are seen to be practically promising for hydrogen (H$_2$) production with high current density (*1*, *2*). In PEMWE, the anodic oxygen evolution reaction (OER) is more inert together with a higher overpotential than the cathodic hydrogen evolution reaction. An anodic catalyst loading as high as 2 to 5 mg$_{Ir}$ cm^{-2} to achieve high energy efficiency is usually required, which contradicts the low global production of Ir and limits PEMWE development (*2–4*). In addition, because of the harsh acidic and polarized environment, iridium oxides–based materials are unsatisfactory because of poor activity of crystalline rutile IrO$_2$ or poor stability of amorphous IrO$_x$. Typically, IrO$_2$ with a high crystallinity exhibits poor activity in OER (*5–7*). For example, rutile IrO$_2$ usually has a greater higher overpotential compared with other active OER catalysts such as RuO$_2$, leading to a high cell voltage and high loading requirement (*5*). Amorphous IrO$_x$ exhibits increased active sites and activity while exhibiting inferior stability (*6*, *8*). A rational design for IrO$_2$ catalysts with balance (trade-off) between activity and stability is therefore critical for continued development of practical low-Ir loaded PEMWEs (*9*, *10*).

The activity and stability of IrO$_2$ are predicated on electrocatalytic mechanisms, e.g., adsorbate evolution mechanism (AEM) and lattice oxygen mechanism (LOM). Rutile IrO$_2$ with high crystallinity has robust Ir—O bonds and therefore follows conventional AEM in which the oxygen molecule is generated from adsorbed water

molecules (*11*, *12*). However, it has a theoretical overpotential of as high as 0.37 V, leading to high energy consumption (*13*). Substantial research is reported to boost activity; however, restriction of the inherent reaction mechanisms limits the improvement (*14*). Alternatively, activating lattice oxygen in IrO$_2$ is feasible for boosting OER activity (*15*). For example, amorphous IrO$_x$ exhibits a substantially boosted catalytic activity in comparison with thermodynamically stable rutile IrO$_2$ via triggering lattice-oxygen oxidation where unsaturated coordination oxygen atoms with weak Ir—O bonding are readily activated for OER (*6*, *16*). However, LOM initiates Ir—O bonding, leading to the accelerated degradation of electrocatalysts (*17–19*). As a result, conventional AEM limits activity, while LOM reduces stability of IrO$_2$-based catalysts. It is important therefore to find a balance, or practical trade-off for behavior of oxygen exchange and to modify the reaction mechanism to involve more active lattice oxygen species in the reaction while maintaining a stable crystal structure (*8*).

Here, we demonstrate a lattice water–assisted short-range ordered iridium oxide (IrO$_x$·nH$_2$O) as an OER electrocatalyst for highly stable acidic water oxidation. The developed IrO$_x$·nH$_2$O has a hollandite-like crystalline with abundant edge-sharing IrO$_6$ octahedrons that accommodates structural water in its lattice, as lattice water, that contrasts with conventional crystalline or amorphous IrO$_2$. We confirm via in situ characterizations that the lattice water is active oxygen species in sustainable and rapid oxygen exchange during OER and contributes to a modified lattice water–assisted pathway that is different to conventional AEM and LOM. As a result, we evidence that the IrO$_x$·nH$_2$O electrocatalyst exhibits notably boosted activity to rutile IrO$_2$ and durability to amorphous IrO$_x$. We confirm that the catalyst exhibits no apparent degradation following 5700 hours (~8 months) of test in a three-electrode cell in 0.1 M HClO$_4$, and importantly, that it maintains excellent activity following 600 hours of pure water PEMWE operation at 60°C (at 1 A cm^{-2}) with less Ir loading than a commercial membrane electrode

[1]School of Chemical Engineering, The University of Adelaide, Adelaide, SA 5005, Australia. [2]Institute for Sustainability, Energy and Resources, The University of Adelaide, Adelaide, SA 5005, Australia. [3]Research School of Chemistry, The Australian National University, Canberra, ACT 2600, Australia. [4]School of Chemistry, Chemical Engineering and Life Sciences, Wuhan University of Technology, Wuhan 430070, China.
*Corresponding author. Email: yao.zheng01@adelaide.edu.au (Y.Z.); s.qiao@adelaide.edu.au (S.-Z.Q.)
†These authors contributed equally to this work.

assembly (MEA). We conclude that lattice water–assisted oxygen exchange is of practical benefit in design of anodic electrocatalysts for high-performance PEMWEs.

RESULTS

Structure analyses

$IrO_x \cdot nH_2O$ was synthesized via a modified molten-salt method with rapid oxidation of $IrCl_3 \cdot nH_2O$ in molten sodium nitrate under 360°C (20, 21). A nanoparticle with a considerably smaller size than that for commercial rutile IrO_2 (IrO_2-CR, control sample) is obtained (fig. S1). An additional control sample, amorphous IrO_x (IrO_x-AM), that was synthesized did not exhibit regular morphology because of low crystallinity. The difference in crystallinity between the three IrO_2-based samples is clear from x-ray diffraction (XRD) patterns. As is shown in Fig. 1A, $IrO_x \cdot nH_2O$ just shows three broad peaks. One peak ca. 5° confirms particle size of ca. 2 nm, which was consistent with the transmission electron microscopy (TEM) image (fig. S2). The other two broad peaks are apparent at ca. 34.4° and 59.0°, which is similar to amorphous IrO_x-AM, while the positions are close to the main peaks of rutile IrO_2-CR. These findings evidence that $IrO_x \cdot nH_2O$ with notably small particle size does not contain long-range ordered crystalline structure.

To determine the local structure, synchrotron-based powder diffraction (PD) with pair-distribution function (PDF) analysis was conducted (fig. S3) (22). As is seen in Fig. 1B, the PDF $G(r)$ for $IrO_x \cdot nH_2O$ is different to that reported crystalline IrO_2 (23), where clearly defined peaks can be found only at low r range, confirming short-range ordered characteristics. Although a low r range contains termination ripples arising from limited Q-range, the local structures can be analyzed from the three sharp pair correlation peaks <4 Å. The first peak ca. 2.04 Å is derived from the Ir-O pairs in IrO_6 octahedra. The second peak at 3.09 Å evidences the edge-sharing Ir-Ir pairs within two neighbored IrO_6 octahedra. The third peak, assigned to corner-sharing Ir-Ir pairs, positively shifts to 3.59 Å with increasing r. The intensity ratio for the edge- and corner-sharing Ir-Ir peaks for $IrO_x \cdot nH_2O$ confirms that the building blocks for $IrO_x \cdot nH_2O$ contain more edge-sharing IrO_6 octahedra in contrast to the rutile structure that is dominated by the corner-sharing IrO_6 octahedral (23). A hollandite-like structure (fig. S4) fits the $IrO_x \cdot nH_2O$ PDF data with good consistency within the 8-Å coherent domain size (Fig. 1B). The hollandite-like framework exhibits tunnels with a size of ca. 7 Å (24) that are confirmed in the high-angle annular dark-field scanning transmission electron microscopy (HAADF-STEM) image (Fig. 1C). The vibration of bonds between Ir and O was determined via Raman spectra (fig. S5). $IrO_x \cdot nH_2O$ exhibits similar vibrations to crystalline IrO_2-CR, while the mode for B_{2g} is negatively shifted and the intensity of A_{1g} is decreased. These findings are attributed to its unique nanostructure nature with the stretched Ir—O bonds (25). IrO_x-AM with the lowest crystallinity exhibited no apparent vibrations. These findings evidence that $IrO_x \cdot nH_2O$ is composed of short-range ordered hollandite-like clusters that are different to the conventional crystalline IrO_2 and amorphous IrO_x.

Identification of structural lattice water molecules

The former structure analyses suggest a hollandite-like framework for $IrO_x \cdot nH_2O$, which may host hydronium ions (defined as lattice water) in the tunnel to maintain thermodynamical stability of the whole framework (23). During the rapid molten salt synthesis, the concentration of water molecules in the muffle furnace increases as temperature rises. The absolute humidity of the muffle furnace at 360°C is greater than that at the initial temperature, 25°C (20), so the water molecules from the air can be readily incorporated into the reaction and enter the framework to balance the charge density and stabilize the structure. On the basis of this conjecture, the presence of lattice water was evidenced with findings from selected spectrometric technologies. Fourier transform infrared (FTIR) spectroscopy spectra show two characteristic peaks for water recorded for $IrO_x \cdot nH_2O$ (Fig. 1D), which are similar to IrO_x-AM. One broad peak appears between 3600 and 3200 cm^{-1} and is attributed to the stretching of O-H and another peak at 1633 cm^{-1} is attributed to the bending of O-H. There are no signals of lattice water for IrO_2-CR. Thermogravimetric analysis coupled with mass spectrometry (TGA-MS) confirms two mass loss stages for $IrO_x \cdot nH_2O$. They are at 100° to 200°C and 200° to 500°C and are attributed to, respectively, the desorption of adsorbed water and loss of lattice water (Fig. 1E) (26). The ^1H magic angle spinning solid-state nuclear magnetic resonance (ssNMR) spectrum for $IrO_x \cdot nH_2O$ confirmed existence of lattice water with a strong proton signal at 3.26 ppm (Fig. 1F). Note that it contains three tiny shoulder peaks (1.26, 0.95, and 0.54 ppm) that are likely contributed by different coordinated water in the lattice.

Importance of lattice water for structural stability

To reveal the significance of lattice water for structural stability of the unique $IrO_x \cdot nH_2O$ framework, we annealed a fresh sample of $IrO_x \cdot nH_2O$ at 500°C for 2 hours in air to remove lattice water (fig. S6, resultant sample is IrO_x). PD data and PDF analysis of IrO_x demonstrate that the unique hollandite-like framework has collapsed and is converted to a general rutile phase, without the lattice water (Fig. 1G and fig. S7). The particle size of resultant IrO_x without lattice water is quite larger than the pristine sample observed in the TEM images (Fig. 1H). The O K-edge characteristics from x-ray absorption near edge structure (XANES) for $IrO_x \cdot nH_2O$ exhibit one only pre-edge peak at 529.8 eV, that is negatively shifted by 0.2 eV from 530 eV for O^{2-}. Following removal of the lattice water, the O K-edge of IrO_x positively shifts back to 530 eV, which is a finding consistent with crystalline IrO_2 (Fig. 1I). The coordination of lattice water likely leads to the slight negative shift of O K-edge in $IrO_x \cdot nH_2O$ (26, 27), which is different from the amorphous IrO_x with an extra signal at 529 eV attributed to active lattice oxygen (28). These findings together confirm the unique role of lattice water in stabilizing the unique short-range, ordered hollandite-like $IrO_x \cdot nH_2O$.

Electrocatalytic OER performance

OER activity and stability for the three IrO_2-based samples, with differing local structure, were assessed in a three-electrode system in O_2-saturated 0.1 M $HClO_4$. The amorphous IrO_x-AM exhibits greatest electrochemical active surface area (ECSA) normalized specific activity (Fig. 2A and figs. S8 and S9). However, performance decays rapidly in <16 hours at 10 mA cm^{-2} in a chronopotentiometry test (Fig. 2B). The crystalline IrO_2-CR exhibits good stability and poor activity. $IrO_x \cdot nH_2O$ exhibits greater specific activity than IrO_2-CR and notably better stability than IrO_x-AM, in which the overpotential at 10 mA cm^{-2} exhibits no apparent increase following 5700 hours (~8 months). In addition, the stability under large
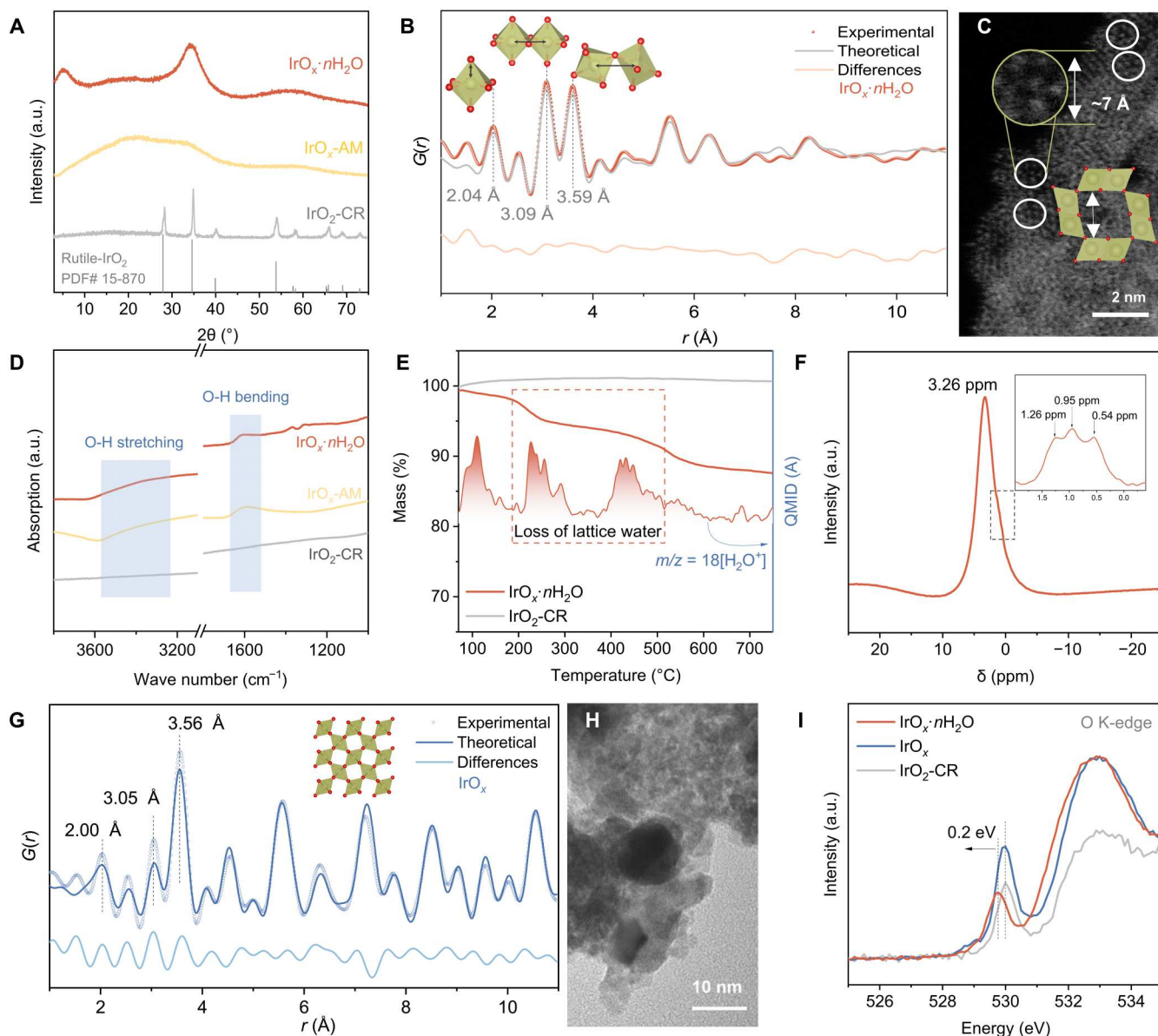
**Fig. 1. Structural analyses.** (**A**) XRD patterns of $IrO_x \cdot nH_2O$, IrO_x-AM and IrO_2-CR. a.u., arbitrary units. (**B**) PDF of $IrO_x \cdot nH_2O$ from PD data and theoretical calculations. (**C**) HAADF-STEM image of $IrO_x \cdot nH_2O$ with structure schematic for $IrO_x \cdot nH_2O$ inserted. (**D**) FTIR spectra of $IrO_x \cdot nH_2O$, IrO_x-AM and IrO_2-CR. (**E**) TGA curves of $IrO_x \cdot nH_2O$ (with coupled MS signals) and IrO_2-CR. QMID, quadrupole multiple ion detection. (**F**) ^1H magic angle spinning ssNMR spectrum of $IrO_x \cdot nH_2O$. (**G**) PDF of IrO_x. (**H**) TEM image of IrO_x. (**I**) Ex situ soft x-ray spectroscopic measurements at O K-edge of $IrO_x \cdot nH_2O$, IrO_x and IrO_2-CR.

current (at 50 mA cm^{-2}) has been further confirmed in fig. S10 that no apparent performance decreases after 200 hours. This is greater stability than even for most reported rutile IrO_2-CR, and to our best knowledge, this is one of the most stable iridium oxides–based acidic OER electrocatalysts reported (table S1) (6, 8, 29–38). The difference in Tafel slope evidences that $IrO_x \cdot nH_2O$ has a different reaction mechanism to conventional amorphous IrO_x-AM (e.g., LOM) and crystalline IrO_2-CR (e.g., AEM) (fig. S11). In addition, $IrO_x \cdot nH_2O$ exhibits the greatest mass activity with more abundant active sites (fig. S12A). Activity for different loadings of $IrO_x \cdot nH_2O$ and IrO_2-CR was determined in fig. S12B. No apparent change in performance is found at a tripled loading of $IrO_x \cdot nH_2O$. This

confirms that even with a low loading of $IrO_x \cdot nH_2O$, a high activity is exhibited that is more efficient than crystalline IrO_2-CR with a high loading. After removal of the lattice water, both the ECSA and intrinsic activity of each active site are decreased with the IrO_x sample (fig. S13).

It is regarded generally that the consumption of unsaturated lattice oxygen during OER in amorphous IrO_x results in fast dissolution of coordinated Ir under the polarization that leads to the poor stability (8, 19, 39). Therefore, the content of Ir dissolved from $IrO_x \cdot nH_2O$ in the anode electrolyte in H-cell was determined via inductively coupled plasma MS (ICP-MS). As is shown in fig. S14, a negligible dissolved Ir is observed in the electrolyte from
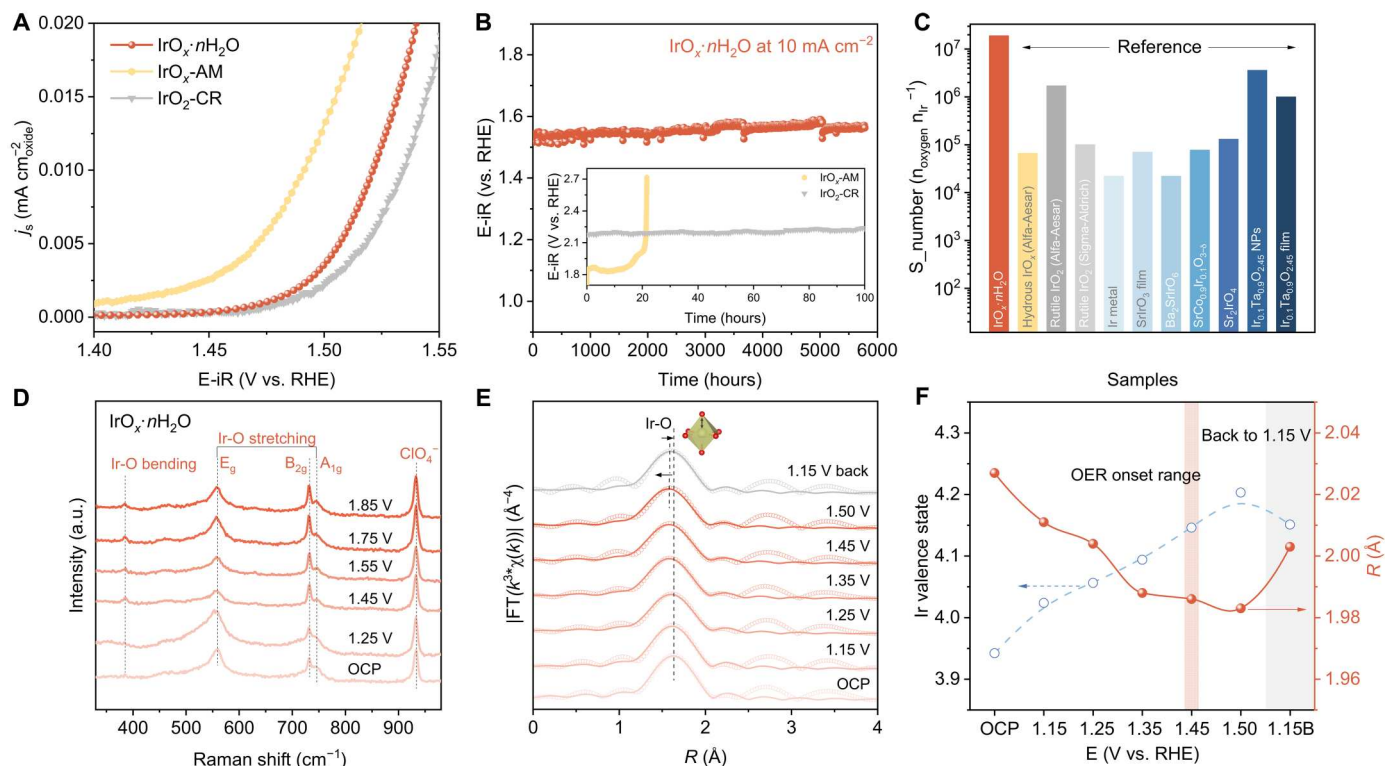
Fig. 2. OER performance and structure characterization during OER. (**A**) ECSA normalized linear sweep voltammetry (LSV) curves. (**B**) Long-term stability of $IrO_x \cdot nH_2O$, IrO_x-AM, and IrO_2-CR. (**C**) S_number calculated from (B) and content of dissolved Ir in electrolyte compared with reported Ir-based electrocatalysts. (**D**) Operando Raman spectra recorded in potential range of OCP ~1.85 V versus RHE for $IrO_x \cdot nH_2O$. (**E**) k^3-weighted operando FT-EXAFS profiles of $IrO_x \cdot nH_2O$ with no phase correction (circle, experimental data; line, fitted data). (**F**) Change in Ir valence state and Ir-O distance of $IrO_x \cdot nH_2O$ as a function of applied potential.

the anodic cell up to 3000 hours. The stability number (S_number) of $IrO_x \cdot nH_2O$ is evaluated as a metric for electrocatalyst stability by calculating from the evolved oxygen gas per dissolved Ir atom in the electrolyte (*18*). As is seen in Fig. 2C, the S_number of $IrO_x \cdot nH_2O$ is as record high as 1.9×10^7 n_{oxygen} n_{Ir}^{-1}, which is two orders of magnitude greater than that of commercial amorphous IrO_x of $(6.6 \times 10^4$ n_{oxygen} $n_{Ir}^{-1})$ (*18, 33, 40*). This finding confirms that superior stability of the short-range ordered lattice water–incorporated $IrO_x \cdot nH_2O$ originates from a different mechanism from LOM that exhibits no dissolution of Ir compared with conventional amorphous IrO_x.

In situ Raman spectra are presented as Fig. 2D and were determined to establish the structural change of $IrO_x \cdot nH_2O$ with increasing OER potential. As applied potential is increased to 1.85 V versus RHE (reversible hydrogen electrode), the bending and stretching modes of Ir—O bonds are maintained at the same position and no potential-dependent peaks appear, evidencing stable Ir-O structure of $IrO_x \cdot nH_2O$. The post-test on the valence of O and Ir in $IrO_x \cdot nH_2O$ was conducted via, respectively, soft x-ray spectroscopy and x-ray absorption spectroscopy (XAS) (fig. S15). The O K-edge of $IrO_x \cdot nH_2O$ following OER is consistent with the fresh sample with a pre-edge peak at 529.8 eV, with no positive or negative shifts observed. This finding confirms the unique short-ranged framework accommodated with lattice water notably remains following OER. A meaningful "slight" decrease in intensity in the white-line peak for Ir L_3-edge of $IrO_x \cdot nH_2O$ after OER was found that is likely the result of dynamical exchange of lattice water

under potential. The hollandite-like structure after OER is apparent in the HAADF image (fig. S16). These findings confirm the stability of $IrO_x \cdot nH_2O$ in OER.

Operando XANES spectra were recorded under potential from open-circuit potential (OCP) to 1.50 V versus RHE to monitor structure evolution of $IrO_x \cdot nH_2O$ during OER in Fig. 2E (see setup in fig. S17). The valence change of Ir is determined via the intensity shift of the white-line peak (fig. S18), which increases with increased applied potential and recovers to a lower value following decrease of the bias to 1.15 V versus RHE (Fig. 2F), evidencing the stable structure of $IrO_x \cdot nH_2O$ coordinated with lattice water. The Ir—O bond change was assessed via fitting the Ir L_3-edge Fourier transforms of extended x-ray absorption fine structure (FT-EXAFS) for $IrO_x \cdot nH_2O$ under differing potential (Fig. 2F, fig. S19, and table S2). The Ir—O bond "shrinks" from 2.027 to 1.983 Å when the potential increases from OCP to 1.50 V versus RHE. Following application of potential back to 1.15 V versus RHE, the bond changes to 2.003 Å; however, it does not recover to 2.011 Å (@1.15 V versus RHE). It is concluded therefore that the volume of the framework is slightly enlarged and stabilized because of shrinkage of I—O under electrochemical polarization that accommodates more water than the initial state. Operando XANES findings evidence the slightly decreased oxidation state of Ir following OER, which is likely the result of increased coordinated water from the dynamic and sustainable exchange from electrolyte under the bias.

Role of lattice water in OER

$IrO_x \cdot nH_2O$ with lattice water exhibits substantially boosted activity and stability. The role of lattice water in OER was established via in situ FTIR spectra (Fig. 3, A to C), and online differential electrochemical MS (DEMS) measurement (Fig. 3, D to F, and fig. S20). In the in situ FTIR spectra of $IrO_x \cdot nH_2O$ (Fig. 3A), in addition to two interfacial water peaks near 3460 and 1648 cm^{-1}, an apparent signal peak near wave number 1222 cm^{-1} is observed under a potential of 1.45 V (versus RHE). It increases with potential that is attributed to generation of *OOH (41). This trend is similar to that for behavior of rutile IrO_2-CR (Fig. 3B) that follows conventional AEM. For amorphous IrO_x-AM (Fig. 3C), there are no signals of *OOH at 1.45 V, even though the current surpasses that of the IrO_2-CR (Fig. 3G). As potential increases, a broad peak appeared at 1000

to 1100 cm^{-1} that is attributed to the signal of *OO (42), evidencing dominance of LOM in IrO_x-AM under low overpotential. *OOH is observed when the potential is 1.50 V because high potential promotes AEM. Notably, the appearance of *OOH intermediates without *OO on $IrO_x \cdot nH_2O$ evidences that it follows a mechanism similar to AEM in which oxygen is generated from one water molecule dissociating and *O combining with another dissociated water molecule to form *OOH, and oxygen is released (43). As is seen in Fig. 3G, the intensity of *OOH recorded on $IrO_x \cdot nH_2O$ is considerably stronger than that recorded for IrO_2-CR following conventional AEM and IrO_x-AM dominated by conventional LOM at potential of 1.45 V, evidencing faster oxygen exchange on $IrO_x \cdot nH_2O$.
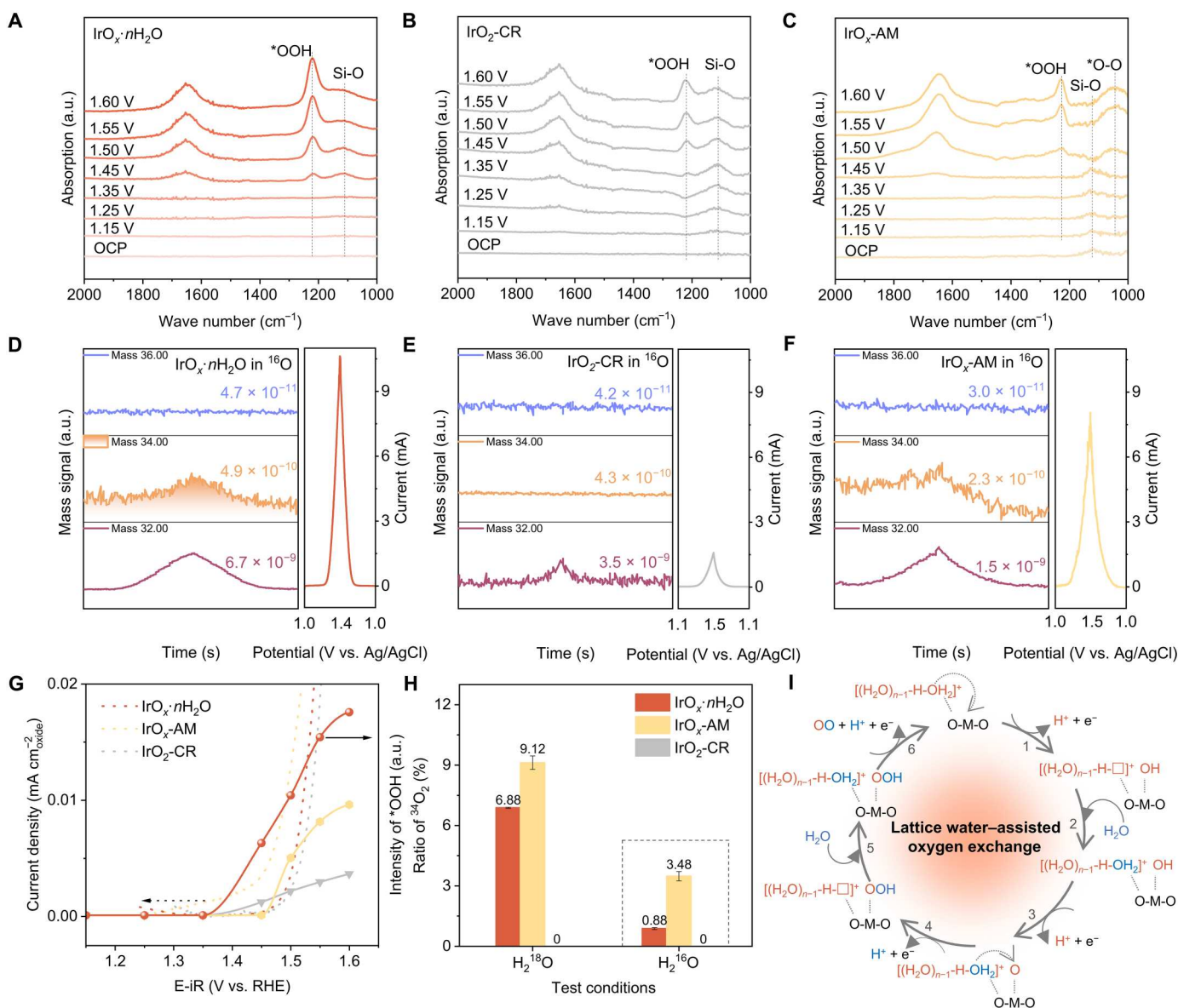
Fig. 3. OER mechanism. In situ FTIR spectra in potential range of OCP ~1.6 V versus RHE of, (**A**) $IrO_x \cdot nH_2O$, (**B**) IrO_2-CR, and (**C**) IrO_x-AM. Online DEMS signal of O_2 products for $IrO_x \cdot nH_2O$ with corresponding CV curve for (**D**) $IrO_x \cdot nH_2O$, (**E**) IrO_2-CR, and (**F**) IrO_x-AM. (**G**) Intensity of *OOH intermediate at different potentials. (**H**) Ratio of $^{34}O_2$ in 0.05 M H_2SO_4 using $H_2^{18}O$ or $H_2^{16}O$ as solvents obtained on $IrO_x \cdot nH_2O$, IrO_x-AM, and IrO_2-CR from DEMS results. (**I**) Schematic for oxygen evolution.

Online DEMS combining isotope labeling was applied to establish the role of lattice water in oxygen exchange and formation of oxygen molecules. Oxygen products including $^{32}O_2(^{16}O^{16}O)$, $^{34}O_2(^{16}O^{18}O)$, and $^{36}O_2(^{18}O^{18}O)$ were collected and analyzed to confirm the source of oxygen in generated oxygen molecules, either from external adsorbed water or from the lattice in the oxides. These experiments were carried out in two steps, namely, step 1 is to make ^{18}O labeling on the oxygen of $IrO_x \cdot nH_2O$, IrO_x-AM, and IrO_2-CR in both lattice oxygen and lattice water by cyclic voltammetry (CV) scanning in the electrolyte with $H_2^{18}O$ as solvent (fig. S20). In this step, $^{36}O_2$ is the main component of anodic gas products together with some $^{34}O_2$ derived from the impurity ^{16}O of $H_2^{18}O$ and the oxygen from the oxides. As presented in Fig. 3H, $^{34}O_2$ obtained with $IrO_x \cdot nH_2O$ as OER electrocatalyst shows a ratio of 6.88%, while that for IrO_x-AM is 9.12% and for IrO_2-CR exhibits zero $^{34}O_2$. These findings evidence that different oxygen from oxides of $IrO_x \cdot nH_2O$ and conventional amorphous IrO_x-AM are involved in the oxygen exchange.

Step 2 is to determine how much labeled oxygen from the catalysts participates in OER under 0.05 M H_2SO_4 ($H_2^{16}O$ as solvent) with the labeled $IrO_x \cdot nH_2O$ and control samples from step 1. As can be seen (Fig. 3, D to F and H), 0.88% of $^{34}O_2$ is obtained with $IrO_x \cdot nH_2O$, which is substantially less than that for IrO_x-AM of 3.48% and more than that for rutile IrO_2-CR of 0%. The higher ratio of $^{34}O_2$ from amorphous IrO_x-AM is attributed to the participation of lattice oxygen in OER as LOM occurs. For the rutile IrO_2-CR, with only AEM happens, adsorbed water only is involved in oxygen evolution, and no labeled oxygen in oxides is available to support oxygen exchange. The IrO_x sample after removing lattice water confirmed that rutile iridium oxide without lattice water incorporated follows a conventional AEM mechanism, in which no lattice oxygen is involved in oxygen evolution, excluding a natural $^{34}O_2$ ratio of 0.21% because of 0.2% natural abundance of $H_2^{18}O$ (44) (fig. S21). For $IrO_x \cdot nH_2O$, as is confirmed in the in situ IR spectra, the presence of *OOH evidences AEM-like route and rules out conventional LOM, and a higher $^{34}O_2$ derived from the labeled oxygen of $IrO_x \cdot nH_2O$ is specially assigned the ^{18}O source to the labeled lattice water.

On the basis of these findings from in situ FTIR and online DEMS, we hypothesize a modified mechanism with lattice water–assisted oxygen exchange for $IrO_x \cdot nH_2O$ in acid OER (Fig. 3I) that is different to conventional AEM and LOM. Namely, initially lattice water is accommodated in the framework of $IrO_x \cdot nH_2O$ in the form of hydronium ions, which are readily nucleophilic attacked by adsorbed water under anodic potential (23). When the OER initiates, the lattice water molecules close to the active site (Ir), marked in orange-color in Fig. 3I, can easily move to the metal site and be dissociated to form *OH intermediates to participate in following oxygen exchange. This leaves a vacant position for the subsequent nucleophilic attack of water from electrolyte (step 1). The external adsorbed water rapidly fills the vacant position of dissociated lattice water to stabilize the structure (step 2), and the newly filled water is dissociated rapidly to generate oxygen molecules on Ir as illustrated in steps 3 to 6, which are similar to AEM route. Notably, step 1 is similar to that in LOM, in that the lattice water directly participates in oxygen exchange, thereby boosting the intrinsic activity of $IrO_x \cdot nH_2O$. However, the lattice water is sustainably supplied so that the structure of $IrO_x \cdot nH_2O$ maintains excellent durability, in contrast to conventional LOM that occurs with unrecoverable

destruction on catalysts. Therefore, a faster and more sustainable oxygen exchange than with conventional AEM and LOM occurs with support of lattice water to deliver measurable boosted activity and stability.
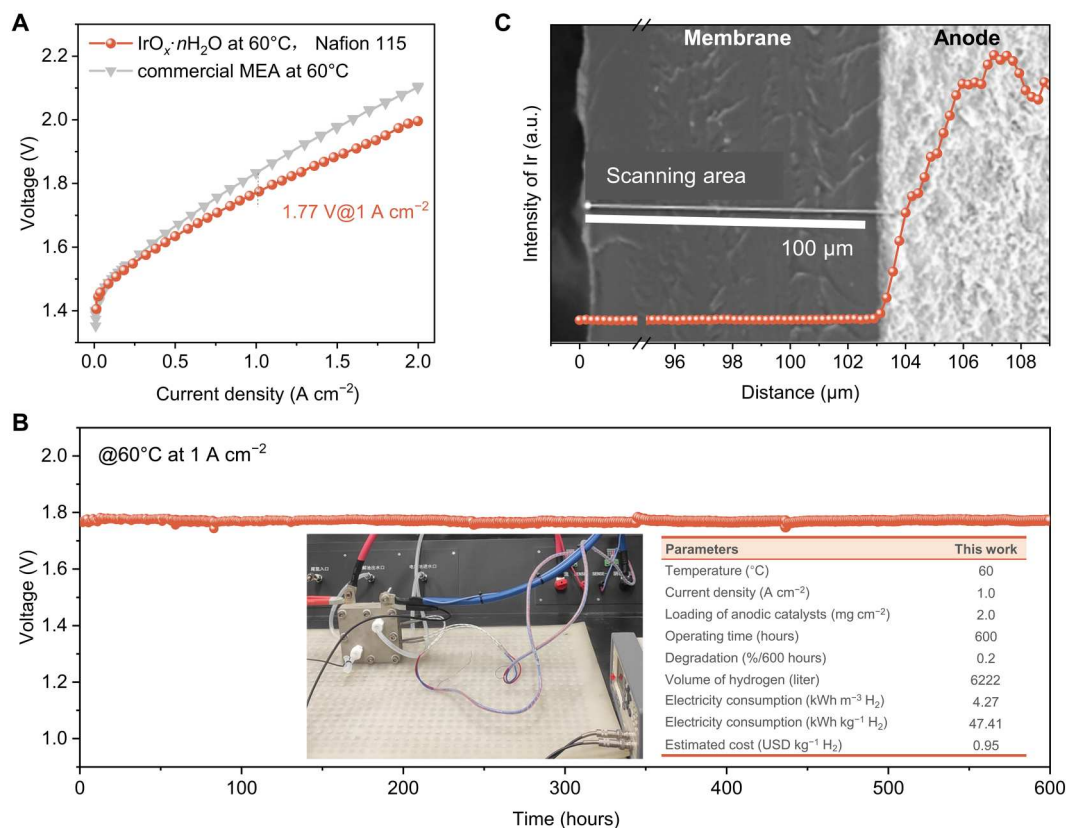
PEMWE performance

Performance of $IrO_x \cdot nH_2O$ was demonstrated in a commercial PEM electrolyzer at 60°C for deionized (DI) water splitting. The electrolyzer is shown as fig. S22. The MEA was customized with an anodic $IrO_x \cdot nH_2O$ loading of 2 mg cm^{-2} on Nafion 115 and 3 mg cm^{-2} of platinum-black coated on the cathode. A commercial MEA was prepared for direct comparison with 3 mg cm^{-2} of IrO_2 in the anode. With less loading of $IrO_x \cdot nH_2O$ working as anodic catalysts, the customized MEA exhibits a cell voltage of 1.77 V at 1 A cm^{-2}, which outperforms the commercial MEA by 60 mV (Fig. 4A). $IrO_x \cdot nH_2O$ exhibits highly substantial stability in PEM applications, with no apparent increase (ca. 0.2%/600 hours) in cell voltage at 1 A cm^{-2} following 600 hours to produce 0.56 kg [6222 liters at standard temperature and pressure (STP)] of H_2 as is seen from Fig. 4B. The energy consumption is just 4.27 kWh m^{-3} H_2 (equated to 47.41 kWh kg^{-1} H_2) at 1.0 A cm^{-2}, which is less than that for reported commercial PEM electrolyzers of 4.5 to 5.0 kWh m^{-3} H_2 (50 to 55.56 kWh kg^{-1} H_2) (45). The estimated cost of this PEMWE is USD 0.95 per kg H_2 (37), which is close to the 2030 goal of USD 1.0 per kg H_2 of the US Hydrogen Earthshot initiative (46). A comparative summary of PEMWE performance between $IrO_x \cdot nH_2O$ with selected typical anodic electrocatalysts is presented as table S3 (37, 38, 47–51). These findings combined confirm the short-range ordered $IrO_x \cdot nH_2O$ with modified oxygen exchange assisted by lattice water is practical for PEMWE.

Following operation at 1 A cm^{-2} for 600 hours, the post-test for $IrO_x \cdot nH_2O$ in MEA was determined via Raman spectroscopy (fig. S23). A similar Raman spectrum for $IrO_x \cdot nH_2O$ was collected that exhibited the same vibrations of Ir—O bonds as prior to the PEMWE test. This finding evidences that there is no apparent structural change following PEMWE operation. As the dispersed nanoparticles and a diffuse layer of Ir after prolonged operation of the PEMWE at high current densities have been previously reported in the catalyst/membrane interface (52), the dissolution and precipitation of Ir species were thus determined via a scanning electron microscope (SEM) and energy-dispersive spectrometer (EDS) (Fig. 4C). No dispersed Ir nanoparticles signals were detected in the SEM cross section. This finding confirms a negligible dissolution of Ir following operation of PEMWE at 1 A cm^{-2} for 600 hours. It is concluded therefore the short-range ordered $IrO_x \cdot nH_2O$, with a modified mechanism assisted by lattice water, is stable in PEMWE under high current density, making it attractive for application in practical devices.

DISCUSSION

In summary, we demonstrate a short-range ordered $IrO_x \cdot nH_2O$ that combines advantage of crystalline and amorphous IrO_2 for an active and durable OER. PDF, together with in situ spectroscopic analyses, evidence that the $IrO_x \cdot nH_2O$ has a hollandite-like framework that accommodates abundant lattice water. The lattice water sustainably participates in oxygen exchange so that OER activity is highly notably boosted without apparent attenuation following 5700 hours (~8 months) under polarization. With the modified oxygen

Fig. 4. PEM performance. (**A**) Steady-state polarization curves of the PEM electrolyzer using $IrO_x \cdot nH_2O$ and commercial IrO_2 as anodic catalysts coated on Nafion 115 membrane operated at 60°C. (**B**) Chronopotentiometric curve of the PEM electrolyzer using $IrO_x \cdot nH_2O$ with digital photographs of PEMWE device and parameters. (**C**) SEM image of cross section of MEA and signals for Ir near the anode catalyst/membrane interface via EDS linear scanning.

exchange assisted by lattice water, $IrO_x \cdot nH_2O$ maintains stability of crystalline IrO_2 and exhibits concurrently excellent activity of amorphous iridium oxide. In a PEMWE application, $IrO_x \cdot nH_2O$ as anodic catalyst delivers a cell voltage of 1.77 V @ 1 A cm^{-2} maintained for 600 hours. This is with less Ir-loading than commercial MEA and an energy consumption of just 4.27 kWh m^{-3} H_2 at 1.0 A cm^{-2}, together with an estimated cost of USD 0.95 per kg H_2. Lattice water–assisted oxygen exchange is therefore of practical benefit in the design of anodic electrocatalysts for high-performance PEMWE. Findings will be of interest to researchers and manufacturers in design of equipment and applications.

MATERIALS AND METHODS
Chemicals
Iridium(III) chloride hydrate ($IrCl_3 \cdot nH_2O$, reagent grade), sodium nitrate ($NaNO_3$, ReagentPlus, ≥99.0%), lithium hydroxide (LiOH, reagent grade, 98%), and iridium(IV) oxide (IrO_2-CR, 99.9%) were purchased from Sigma-Aldrich. DI water was supplied by the Milli-Q Benchtop laboratory water purification systems (Sigma-Aldrich).

Material synthesis
$IrO_x \cdot nH_2O$ was synthesized via a modified molten-salt method (20, 21). Five grams of $NaNO_3$ was melted at 360°C in a muffle furnace, to which 40 mg of $IrCl_3 \cdot nH_2O$ was added rapidly with continued reaction for 5 min. The crucible was removed and cooled naturally

to room temperature (RT). Salts were removed by DI water, and $IrO_x \cdot nH_2O$ was separated via filtration and dried at 60°C overnight. IrO_x was obtained by annealing $IrO_x \cdot nH_2O$ in air at 500°C for 2 hours, and the lattice water was completely removed.

Amorphous IrO_x-AM was synthesized using reported methods (53). $IrCl_3 \cdot nH_2O$ (120 mg) and 77 mg of LiOH were added to 4 ml of DI water and stirred overnight to generate a blue-color solution. An additional 4 ml of DI water was added, and the mix was heated to reflux for 3 hours. Last, the product was washed with hot DI water thoroughly and dried naturally.

Characterization
XRD data were recorded on a Rigaku MiniFlex 600 XRD using Cu Kα (1.54 Å, 40 kV, 15 mA) x-ray source. PD patterns were collected from the Powder Diffraction beamline at the Australian Synchrotron with the wavelength (λ) of 0.5903 Å. The PDFgetX3 was used to convert the x-ray PD data to the atomic PDF (54). Experimental PDFs were analyzed using the software package, PDFgui (55). O K-edge spectra were collected on the Soft X-ray Spectroscopy beamline at the Australian Synchrotron, and all data were calibrated with reference to the standard foil. HAADF-STEM images were recorded on the aberration-corrected FEI Titan Themis operating at 200 kV. SEM images were collected using a FEI QUANTA 450 FEG Environmental SEM OPERATING at 10 kV. TEM images were recorded on Phillips CM200 operating at 200 kV. TGA-MS analyses were carried out with a NETZSCH STA 449 F5 Jupiter.

TGA-MS was operated via heating ca. 5 mg of sample under high-purity nitrogen with 10 ml min^{-1}, from RT to 750°C at a rate of 5 K min^{-1} (for improved signal). ^{1}H ssNMR spectrum was determined at 700 MHz with a spinning rate of 40 kHz at RT using a Phoenix NMR triple resonance broadband probe. FTIR spectrum for powder (pretreated at 120°C overnight) was collected on a Nicolet 6700 Fourier Transform Infrared Spectrometer. Ex situ Raman spectra were recorded on Renishaw Raman spectroscopy with a 50× objective and a laser wavelength of 532 nm.

Electrochemical characterization

Electrochemical measurements were carried out in a three-electrode system in O_2-saturated 0.1 M $HClO_4$ with a CHI-760E electrochemical workstation under RT. Four milligrams of catalyst was dispersed in a 1 ml of mixture of water and ethanol (AR) ($V_{water}/V_{ethanol} = 4/1$), 40 μl of 5 wt % Nafion solution was added and the mix ultrasonicated for 60 min to obtain a homogeneous ink. The ink (7.6 μl) was dropped on a rotating disk electrode (Pine Research Instrument) with a diameter of 5 mm and dried naturally for the working electrode. For the stability test on fluorine-doped tin oxide (FTO) and platinized titanium felt (for large density test), ca. 200 μl of catalyst was sprayed on an area of 0.5 cm^2, and loading of 1.5 mg cm^{-2} was controlled. A Pt-wire was selected as the counter and Ag/AgCl as the reference electrode. The working electrode was cyclically scanned from 1.0 to 1.55 V (versus RHE) to reach a stable state for pre-activation for OER activity determination. Linear sweep voltammetry curves were collected with a scanning rate of 2 mV s^{-1}. Potentials were corrected by 100% iR compensation. Electrochemical active surface area was estimated from the electrochemical double-layer capacitance (C_{dl}) from Eq. 1 (56). The value for C_{dl} was determined via CV scanning in a non-Faradic region from 1.0 to 1.1 V versus Ag/AgCl with scanning rate, 20, 40, 60, 80, and 100 mV s^{-1}. The current at 1.05 V versus Ag/AgCl exhibited a linear relationship with scanning rate. The value of the slope was determined from fitting of the data to obtain C_{dl}. The specific current density per ECSA (j_s) was computed via normalizing the current by ECSA, namely

$$ECSA = \frac{C_{dl}}{0.035 \text{ mF cm}^{-2}} \quad (1)$$

Mass activity (j_m) was determined from Eq. 2, where j_m is the current density normalized by the geometric area, A_{geo} is the electrode area and m_{Ir} is the iridium loading mass of electrocatalyst on electrode.

$$j_m = \frac{j_{geo} \times A_{geo}}{m_{Ir}} \quad (2)$$

The stability test of the catalyst was determined at a current density of 10 mA cm^{-2} at RT. A stirring bar was used in the electrolyte to remove bubbles from the surface of the electrode and for fast proton transfer during the test. E-t curves were 100% iR-compensated. Commercial crystalline and amorphous IrO_2 were similarly prepared for stability comparison.

Potentials were calibrated to an RHE in H_2-saturated 0.1 M $HClO_4$ (57).

$$E_{RHE} = E_{Ag/AgCl} + 0.25 \text{ V} \quad (3)$$

The stability number (S_number) was computed from Eq. 4 (18)

$$\text{S\_number} = \frac{n_{oxygen}}{n_{iridium}} \quad (4)$$

where n_{oxygen} is the molar number of oxygen produced during a time and $n_{iridium}$ is the molar number of dissolved Ir in electrolyte determined via ICP-MS.

ICP-MS analyses of Ir dissolution

The dissolution of Ir during OER was quantified via ICP-MS (Agilent 8900 ICP-QQQ). An H-cell was applied to separate the working and counter electrode. The working electrode was prepared by spraying the catalyst on FTO with a loading of 1.5 mg cm^{-2}. One hundred milliliters of 0.1 M $HClO_4$ was used as electrolyte. Two milliliters of the electrolyte from the anodic cell following electrolysis (@ 10 mA cm^{-2}) at 0, 0.5, 1, 2, 4, 24, 48, 100, 200 and 3000 hours was collected for ICP-MS measurement.

Online DEMS measurement

DEMS (The Hidden HPR-40 DEMS) was used to determine the OER mechanism combined with ^{18}O isotope labeling. A customized flow cell was used and the electrolyte pumped through the cell at 50 ml min^{-1}. The working electrode was prepared by coating Au onto a polytetrafluoroethylene (PTFE) film. A loading of 0.2 mg cm^{-2} catalyst was dropped on the Au-film and dried at 60°C. A saturated Ag/AgCl was the reference and Pt-wire the counter electrode. For greater purity of H_2^{18}O, we selected 98% H_2SO_4 and diluted it to pH = 1 as the electrolyte for the DEMS isotope labeling. CV scanning in the range 1.0 to 1.4 V ($IrO_x \cdot nH_2O$)/1.50 V(IrO_x-AM, IrO_2-CR) (versus Ag/AgCl) for 5 cycles at a scanning rate of 5 mV s^{-1} was applied under H_2^{18}O supporting 0.05 M H_2SO_4. The working electrode and the whole cell were washed with DI water thoroughly to remove ^{18}O and then dried at 60°C. ^{18}O-labeled electrodes were prepared and CV cycles performed in 0.05 M H_2SO_4 (H_2^{16}O as solvent) with the same potential window and scan rate. During OER, oxygen with different molecular masses was collected and determined via mass spectroscopy. With the signals of $^{34}O_2$, the behavior of oxygen exchange during OER can be established. Experiments were repeated three times.

In situ FTIR

In situ FTIR was carried out on Nicolet iS50 FTIR Spectrometer to determine the potential-dependent intermediates and reaction mechanism. A PIKE jackfish cell was used and O_2-saturated 0.1 M $HClO_4$ was selected as electrolyte. A catalyst loading of 0.2 mg cm^{-2} was dropped on an Au-coated Si ATR wafer, which dried naturally and acted as a working electrode. A saturated Ag/AgCl was the reference and a Pt-wire counter electrode. The background was subtracted under open circuit potential. Spectra between 1000 and 4000 cm^{-1} were collected at differing potential with polarization in advance for at least 5 min to reach a stable current.

In situ Raman spectroscopy

In situ Raman spectroscopy was conducted on Renishaw Raman spectroscopy with a special 60× objective that was immersed in the electrolyte and a laser wavelength of 532 nm. Collection was at 10 s of exposure with 10 exposures. A screen-printed chip electrode from Pine Research Instrumentation was used. Prepared ink (10 μl) was dropped on the chip and dried at RT, and 0.1 M $HClO_4$

was applied as electrolyte. Spectra were collected following removal of bubbles at different potential with polarization in advance for 10 min. Measurement at each potential was carried out at three differing points.

XAS measurement

XAS data were determined with the XAS beamline at the Australian Synchrotron ANSTO. Ex situ XAS measurements were determined via transmission mode in the RT chamber. Operando XAS measurements were determined in three repeats to confirm findings. A homemade operando cell and CHI-760E electrochemical workstation were used. $IrO_x \cdot nH_2O$ loaded on carbon paper was used as the working electrode. Ag/AgCl was used as the reference and Pt-wire as counter electrode. Oxygen-saturated 0.1 M $HClO_4$ electrolyte was pumped through the cell at 50 ml min^{-1} to remove any in situ generated bubbles. Operando Ir-L_3 XANES and FT-EXAFS spectra were recorded in fluorescence mode at RT. Data were analyzed and processed via Athena and Artemis software following standard procedure using the Demeter program package (0.9.26) (58).

PEM measurement

The PEMWE measurements were conducted via the test system, JNR (Wuhan Jingneng Electronic Technology Co., Ltd.). Catalysts were prepared as a MEA with an anodic loading of 2 mg cm^{-2} ($IrO_x \cdot nH_2O$) on Nafion 115 and 3 mg cm^{-2} of Pt black coated on the cathode. A commercial MEA was purchased from Fuel Cell Store for comparison with 3 mg cm^{-2} of IrO_2 coated on the anode and 3 mg cm^{-2} of Pt black coated on the cathode. The cell was integrated via pressing two Ti bipolar plates, diffusion layers, and MEA. A Ti-fiber felt (0.25-mm thickness, 78% porosity, Bekaert) was used as the anodic gas diffusion layer (GDL), and carbon paper (TGP-H-060, Toray Industries, Inc) as the cathodic GDL. The active area of MEA was controlled at 25 cm^2 (5 cm*5 cm). For the PEM test, the temperature was controlled at 60°C, and preheated DI water (18.2 Mohm cm, 25°C) was kept flowing through the cell at 50 ml min^{-1}. The water was added to fill a 10-liter tank of the test system and was supplemented per 5 days. Activation was carried out prior to the test with a prepolarization at 1 A cm^{-2} for 1 hour. The steady-state polarization curve was determined via the galvanostatic method, and each point was recorded until the cell voltage was stable. The stability test in PEM ran at 1 A cm^{-2} for 600 hours.

Determination of dissolved and precipitated Ir in MEA

The post-test of MEA for determination of dissolution and precipitation of Ir was conducted using SEM-EDS. The MEA cut-outs were immersed in liquid nitrogen for 1 min to obtain brittle fracture. The fracture was prepared for SEM imaging by carbon coating. Elemental mapping by EDS with linear scanning at an acceleration voltage of 20 kV was used to record dissolved Ir species in the membrane.

Estimation of hydrogen produced and cost in PEMWE

The calculation of hydrogen cost in PEMWE was based on (37). Specifically,

$$\text{Mass of } H_2 = \frac{j(\text{current density}) \times A(\text{electrolyzer area}) \times t\,(\text{working time}) \times \text{Molar mass } H_2}{2 \times F}$$

$$= \frac{1\,\text{A cm}^{-2} \times 25\,\text{cm}^2 \times 600\,\text{hours} \times 3600\,\frac{\text{hours}}{\text{s}} \times 2\,\text{g mol}^{-1}}{2 \times 96485\,\text{c mol}^{-1}} = 560\,\text{g} \tag{5}$$

$$\text{Volume of } H_2 = \frac{m}{\rho} = \frac{560\,\text{g}}{0.09\,\text{g liter}^{-1}} = 6222\,\text{liters} \tag{6}$$

$$\text{Energy consumption} = \frac{1.77\,\text{V} \times 25\,\text{A} \times 600\,\text{hours}}{0.56\,\text{kg } H_2} = \frac{47.41\,\text{kWh}}{\text{kg } H_2} = \frac{4.27\,\text{kWh}}{\text{m}^3\,H_2} \tag{7}$$

$$\text{Cost per kilogram of } H_2 = \text{energy consumption} \times \text{electricity bill}$$

$$= \frac{1.77\,\text{V} \times 25\,\text{A} \times 600\,\text{hours}}{0.56\,\text{kg } H_2} \times \frac{\text{USD } 0.02}{\text{kWh}}$$

$$= \frac{\text{USD } 0.95}{\text{kg } H_2} \tag{8}$$

Supplementary Materials

This PDF file includes:
Figs. S1 to S23
Tables S1 to S3

REFERENCES AND NOTES

1. International Energy Agency (IEA), "Electrolyzers" (IEA, 2022); www.iea.org/reports/electrolysers.
2. M. Carmo, D. L. Fritz, J. Mergel, D. Stolten, A comprehensive review on PEM water electrolysis. *Int. J. Hydrog. Energy* **38**, 4901–4934 (2013).
3. Z. C. Chen, L. Guo, L. Pan, T. Q. Yan, Z. X. He, Y. Li, C. X. Shi, Z.-F. Huang, X. W. Zhang, J.-J. Zou, Advances in oxygen evolution electrocatalysts for proton exchange membrane water electrolyzers. *Adv. Energy Mater.* **12**, 2103670 (2022).
4. Y. Jiao, Y. Zheng, M. T. Jaroniec, S. Z. Qiao, Design of electrocatalysts for oxygen- and hydrogen-involving energy conversion reactions. *Chem. Soc. Rev.* **44**, 2060–2086 (2015).
5. T. Reier, H. N. Nong, D. Teschner, R. Schlogl, P. Strasser, Electrocatalytic oxygen evolution reaction in acidic environments - reaction mechanisms and catalysts. *Adv. Energy Mater.* **7**, 1601275 (2017).
6. D. F. Abbott, D. Lebedev, K. Waltar, M. Povia, M. Nachtegaal, E. Fabbri, C. Coperet, T. J. Schmidt, Iridium oxide for the oxygen evolution reaction: Correlation between particle size, morphology, and the surface hydroxo layer from operando XAS. *Chem. Mater.* **28**, 6591–6604 (2016).
7. M. Bernicke, E. Ortel, T. Reier, A. Bergmann, J. Ferreira de Araujo, P. Strasser, R. Kraehnert, Iridium oxide coatings with templated porosity as highly active oxygen evolution catalysts: Structure-activity relationships. *ChemSusChem* **8**, 1908–1915 (2015).
8. A. Lončar, D. Escalera-López, S. Cherevko, N. Hodnik, Inter-relationships between oxygen evolution and iridium dissolution mechanisms. *Angew. Chem. Int. Ed.* **61**, e202114437 (2022).
9. J. Kibsgaard, I. Chorkendorff, Considerations for the scaling-up of water splitting catalysts. *Nat. Energy* **4**, 430–433 (2019).
10. M. F. Lagadec, A. Grimaud, Water electrolysers with closed and open electrochemical systems. *Nat. Mater.* **19**, 1140–1150 (2020).
11. A. Zagalskaya, V. Alexandrov, Role of defects in the interplay between adsorbate evolving and lattice oxygen mechanisms of the oxygen evolution reaction in RuO_2 and IrO_2. *ACS Catal.* **10**, 3650–3657 (2020).
12. A. Zagalskaya, I. Evazzade, V. Alexandrov, *Ab Initio* Thermodynamics and kinetics of the lattice oxygen evolution reaction in iridium oxides. *ACS Energy Lett.* **6**, 1124–1133 (2021).

13. M. T. M. Koper, Theory of multiple proton–electron transfer reactions and its implications for electrocatalysis. *Chem. Sci.* **4**, 2710–2723 (2013).

14. J. Song, C. Wei, Z.-F. Huang, C. Liu, L. Zeng, X. Wang, Z. C. J. Xu, A review on fundamentals for designing oxygen evolution electrocatalysts. *Chem. Soc. Rev.* **49**, 2196–2214 (2020).

15. A. Grimaud, O. Diaz-Morales, B. Han, W. T. Hong, Y.-L. Lee, L. Giordano, K. A. Stoerzinger, M. T. M. Koper, Y. Shao-Horn, Activating lattice oxygen redox reactions in metal oxides to catalyse oxygen evolution. *Nat. Chem.* **9**, 457–465 (2017).

16. R. V. Mom, L. J. Falling, O. Kasian, G. Algara-Siller, D. Teschner, R. H. Crabtree, A. Knop-Gericke, K. J. J. Mayrhofer, J.-J. Velasco-Vélez, T. E. Jones, *Operando* Structure–Activity–Stability relationship of iridium oxides during the oxygen evolution reaction. *ACS Catal.* **12**, 5174–5184 (2022).

17. A. Zagalskaya, V. Alexandrov, Mechanistic study of IrO₂ dissolution during the electrocatalytic oxygen evolution reaction. *J. Phys. Chem. Lett.* **11**, 2695–2700 (2020).

18. S. Geiger, O. Kasian, M. Ledendecker, E. Pizzutilo, A. M. Mingers, W. T. Fu, O. Diaz-Morales, Z. Li, T. Oellers, L. Fruchter, A. Ludwig, K. J. J. Mayrhofer, M. T. M. Koper, S. Cherevko, The stability number as a metric for electrocatalyst stability benchmarking. *Nat. Catal.* **1**, 508–515 (2018).

19. O. Kasian, S. Geiger, T. Li, J.-P. Grote, K. Schweinar, S. Zhang, C. Scheu, D. Raabe, S. Cherevko, B. Gault, K. J. J. Mayrhofer, Degradation of iridium oxides via oxygen evolution from the lattice: Correlating atomic scale structure with reaction mechanisms. *Energ. Environ. Sci.* **12**, 3548–3555 (2019).

20. Z. Hu, X. Xiao, H. Jin, T. Li, M. Chen, Z. Liang, Z. Guo, J. Li, J. Wan, L. Huang, Y. Zhang, G. Feng, J. Zhou, Rapid mass production of two-dimensional metal oxides and hydroxides via the molten salts method. *Nat. Commun.* **8**, 15630 (2017).

21. H. Jin, X. Liu, P. An, C. Tang, H. Yu, Q. Zhang, H.-J. Peng, L. Gu, Y. Zheng, T. Song, K. Davey, U. Paik, J. Dong, S.-Z. Qiao, Dynamic rhenium dopant boosts ruthenium oxide for durable oxygen evolution. *Nat. Commun.* **14**, 354 (2023).

22. T. Egami, S. J. Billinge, *Underneath the Bragg Peaks: Structural Analysis of Complex Materials* (Newnes, 2012).

23. E. Willinger, C. Massué, R. Schlögl, M. G. Willinger, Identifying key structural features of IrOₓ water splitting catalysts. *J. Am. Chem. Soc.* **139**, 12093–12101 (2017).

24. S. Lee, Y.-J. Lee, G. Lee, A. Soon, Activated chemical bonds in nanoporous and amorphous iridium oxides favor low overpotential for oxygen evolution reaction. *Nat. Commun.* **13**, 3171 (2022).

25. A. V. Korotcov, Y.-S. Huang, K.-K. Tiong, D.-S. Tsai, Raman scattering characterization of well-aligned RuO₂ and IrO₂ nanocrystals. *J. Raman Spectrosc.* **38**, 737–749 (2007).

26. R. Zhang, P. E. Pearce, V. Pimenta, J. Cabana, H. Li, D. A. D. Corte, A. M. Abakumov, G. Rousse, D. Giaume, M. Deschamps, A. Grimaud, First example of protonation of ruddlesden–popper Sr₂IrO₄: A route to enhanced water oxidation catalysts. *Chem. Mater.* **32**, 3499–3509 (2020).

27. R. Wirth, Water in minerals detectable by electron energy-loss spectroscopy EELS. *Phys. Chem. Miner.* **24**, 561–568 (1997).

28. V. Pfeifer, T. E. Jones, J. J. Velasco Vélez, C. Massué, M. T. Greiner, R. Arrigo, D. Teschner, F. Girgsdies, M. Scherzer, J. Allan, M. Hashagen, G. Weinberg, S. Piccinin, M. Hävecker, A. Knop-Gericke, R. Schlögl, The electronic structure of iridium oxide electrodes active in water splitting. *Phys. Chem. Chem. Phys.* **18**, 2292–2296 (2016).

29. O. Diaz-Morales, S. Raaijman, R. Kortlever, P. J. Kooyman, T. Wezendonk, J. Gascon, W. T. Fu, M. T. M. Koper, Iridium-based double perovskites for efficient water oxidation in acid media. *Nat. Commun.* **7**, 12363 (2016).

30. L. C. Seitz, C. F. Dickens, K. Nishio, Y. Hikita, J. Montoya, A. Doyle, C. Kirk, A. Vojvodic, H. Y. Hwang, J. K. Norskov, T. F. Jaramillo, A highly active and stable IrOₓ/SrIrO₃ catalyst for the oxygen evolution reaction. *Science* **353**, 1011–1014 (2016).

31. L. Yang, G. Yu, X. Ai, W. Yan, H. Duan, W. Chen, X. Li, T. Wang, C. Zhang, X. R. Huang, J.-S. Chen, X. Zou, Efficient oxygen evolution electrocatalysis in acid by a perovskite with face-sharing IrO₆ octahedral dimers. *Nat. Commun.* **9**, 5236 (2018).

32. J. Chen, P. Cui, G. Zhao, K. Rui, M. Lao, Y. Chen, X. Zheng, Y. Jiang, H. Pan, S. Dou, W. Sun, Low-coordinate iridium oxide confined on graphitic carbon nitride for highly efficient oxygen evolution. *Angew. Chem. Int. Ed.* **58**, 12540–12544 (2019).

33. Y. Chen, H. Li, J. Wang, Y. Du, S. Xi, Y. Sun, M. Sherburne, J. W. Ager, A. C. Fisher, Z. J. Xu, Exceptionally active iridium evolved from a pseudo-cubic perovskite for oxygen evolution in acid. *Nat. Commun.* **10**, 572 (2019).

34. J. Gao, C.-Q. Xu, S.-F. Hung, W. Liu, W. Cai, Z. Zeng, C. Jia, H. Chen, H. Xiao, J. Li, Y. Huang, B. Liu, Breaking long-range order in iridium oxide by alkali ion for efficient water oxidation. *J. Am. Chem. Soc.* **141**, 3014–3023 (2019).

35. Q. Dang, H. Lin, Z. Fan, L. Ma, Q. Shao, Y. Ji, F. Zheng, S. Geng, S.-Z. Yang, N. Kong, W. Zhu, Y. Li, F. Liao, X. Huang, M. Shao, Iridium metallene oxide for acidic oxygen evolution catalysis. *Nat. Commun.* **12**, 6007 (2021).

36. G. Wu, X. Zheng, P. Cui, H. Jiang, X. Wang, Y. Qu, W. Chen, Y. Lin, H. Li, X. Han, Y. Hu, P. Liu, Q. Zhang, J. Ge, Y. Yao, R. Sun, Y. Wu, L. Gu, X. Hong, Y. Li, A general synthesis approach for amorphous noble metal nanosheets. *Nat. Commun.* **10**, 4855 (2019).

37. S. Hao, H. Sheng, M. Liu, J. Huang, G. Zheng, F. Zhang, X. Liu, Z. Su, J. Hu, Y. Qian, L. Zhou, Y. He, B. Song, L. Lei, X. Zhang, S. Jin, Torsion strained iridium oxide for efficient acidic water oxidation in proton exchange membrane electrolyzers. *Nat. Nanotechnol.* **16**, 1371–1377 (2021).

38. Z. Shi, J. Li, J. Jiang, Y. Wang, X. Wang, Y. Li, L. Yang, Y. Chu, J. Bai, J. Yang, J. Ni, Y. Wang, L. Zhang, Z. Jiang, C. Liu, J. Ge, W. Xing, Enhanced acidic water oxidation by dynamic migration of oxygen species at the Ir/Nb₂O₅₋ₓ catalyst/support interfaces. *Angew. Chem. Int. Ed.* **61**, e202212341 (2022).

39. O. Kasian, J.-P. Grote, S. Geiger, S. Cherevko, K. J. J. Mayrhofer, The common intermediates of oxygen evolution and dissolution reactions during water electrolysis on iridium. *Angew. Chem. Int. Ed.* **57**, 2488–2491 (2018).

40. Y.-R. Zheng, J. Vernieres, Z. Wang, K. Zhang, D. Hochfilzer, K. Krempl, T.-W. Liao, F. Presel, T. Altantzis, J. Fatermans, S. B. Scott, N. M. Secher, C. Moon, P. Liu, S. Bals, S. Van Aert, A. Cao, M. Anand, J. K. Nørskov, J. Kibsgaard, I. Chorkendorff, Monitoring oxygen production on mass-selected iridium–tantalum oxide electrocatalysts. *Nat. Energy* **7**, 55–64 (2022).

41. S. Nayak, I. J. McPherson, K. A. Vincent, Adsorbed intermediates in oxygen reduction on platinum nanoparticles observed by in situ IR spectroscopy. *Angew. Chem. Int. Ed.* **57**, 12855–12858 (2018).

42. C. Lin, J.-L. Li, X. Li, S. Yang, W. Luo, Y. Zhang, S.-H. Kim, D.-H. Kim, S. S. Shinde, Y.-F. Li, Z.-P. Liu, Z. Jiang, J.-H. Lee, In-situ reconstructed Ru atom array on α-MnO₂ with enhanced performance for acidic water oxidation. *Nat. Catal.* **4**, 1012–1023 (2021).

43. L. An, C. Wei, M. Lu, H. Liu, Y. Chen, G. G. Scherer, A. C. Fisher, P. Xi, Z. J. Xu, C.-H. Yan, Recent development of oxygen evolution electrocatalysts in acidic environment. *Adv. Mater.* **33**, 2006328 (2021).

44. S. B. Scott, J. E. Sørensen, R. R. Rao, C. Moon, J. Kibsgaard, Y. Shao-Horn, I. Chorkendorff, The low overpotential regime of acidic water oxidation part II: Trends in metal and oxygen stability numbers. *Energ. Environ. Sci.* **15**, 1988–2001 (2022).

45. M. Wang, Z. Wang, X. Gong, Z. Guo, The intensification technologies to water electrolysis for hydrogen production – A review. *Renew. Sustain. Energy Rev.* **29**, 573–588 (2014).

46. International Energy Agency (IEA), "Global Hydrogen Review 2022" (IEA, 2022); www.iea.org/reports/global-hydrogen-review-2022.

47. C. Xu, L. Ma, J. Li, W. Zhao, Z. Gan, Synthesis and characterization of novel high-performance composite electrocatalysts for the oxygen evolution in solid polymer electrolyte (SPE) water electrolysis. *Int. J. Hydrog. Energy* **37**, 2985–2992 (2012).

48. S. A. Grigoriev, P. Millet, S. V. Korobtsev, V. I. Porembskiy, M. Pepic, C. Etievant, C. Puyenchet, V. N. Fateev, Hydrogen safety aspects related to high-pressure polymer electrolyte membrane water electrolysis. *Int. J. Hydrog.Energy* **34**, 5986–5991 (2009).

49. J. Lim, G. Kang, J. W. Lee, S. S. Jeon, H. Jeon, P. W. Kang, H. Lee, Amorphous Ir atomic clusters anchored on crystalline IrO₂ nanoneedles for proton exchange membrane water oxidation. *J. Power Sources* **524**, 231069 (2022).

50. S. Siracusano, N. Van Dijk, E. Payne-Johnson, V. Baglio, A. S. Aricò, Nanosized IrOₓ and IrRuOₓ electrocatalysts for the O₂ evolution reaction in PEM water electrolysers. *Appl Catal B* **164**, 488–495 (2015).

51. G. Li, H. Yu, W. Song, X. Wang, Y. Li, Z. Shao, B. Yi, Zeolite-templated IrₓRu₁₋ₓO₂ electrocatalysts for oxygen evolution reaction in solid polymer electrolyte water electrolyzers. *Int. J. Hydrog. Energy* **37**, 16786–16794 (2012).

52. P. Lettenmeier, R. Wang, R. Abouatallah, S. Helmly, T. Morawietz, R. Hiesgen, S. Kolb, F. Burggraf, J. Kallo, A. S. Gago, K. A. Friedrich, Durable membrane electrode assemblies for proton exchange membrane electrolyzer systems operating at high current densities. *Electrochim. Acta* **210**, 502–511 (2016).

53. J. Ruiz Esquius, D. J. Morgan, I. Spanos, D. G. Hewes, S. J. Freakley, G. J. Hutchings, Effect of base on the facile hydrothermal preparation of highly active IrOₓ Oxygen evolution catalysts. *ACS Appl. Energy Mater.* **3**, 800–809 (2020).

54. P. Juhás, T. Davis, C. L. Farrow, S. Billinge, PDFgetX3: A rapid and highly automatable program for processing powder diffraction data into total scattering pair distribution functions. *J. Appl. Cryst.* **46**, 560–566 (2013).

55. C. L. Farrow, P. Juhas, J. W. Liu, D. Bryndin, E. S. Božin, J. Bloch, T. Proffen, S. J. L. Billinge, PDFfit2 and PDFgui: Computer programs for studying nanostructure in crystals. *J. Phys. Condens. Matter* **19**, 335219 (2007).

56. C. Wei, S. Sun, D. Mandler, X. Wang, S. Z. Qiao, Z. J. Xu, Approaches for measuring the surface areas of metal oxide electrocatalysts for determining their intrinsic electrocatalytic activity. *Chem. Soc. Rev.* **48**, 2518–2534 (2019).

57. S. Niu, S. Li, Y. Du, X. Han, P. Xu, How to reliably report the overpotential of an electrocatalyst. *ACS Energy Lett.* **5**, 1083–1087 (2020).

58. B. Ravel, M. Newville, ATHENA, ARTEMIS, HEPHAESTUS: Data analysis for X-ray absorption spectroscopy using IFEFFIT. *J. Synchrotron Radiat.* **12**, 537–541 (2005).

Science Advances

IrO$_x$-nH$_2$O with lattice water–assisted oxygen exchange for high-performance proton exchange membrane water electrolyzers

Jun Xu, Huanyu Jin, Teng Lu, Junsheng Li, Yun Liu, Kenneth Davey, Yao Zheng, and Shi-Zhang Qiao

View the article online
https://www.science.org/doi/10.1126/sciadv.adh1718
Permissions
https://www.science.org/help/reprints-and-permissions

Use of this article is subject to the Terms of service